∂Pacific Sea Surface Temperature Anomalies as Important Boundary Forcing in Driving the Interannual Warm Arctic–Cold Continent Pattern over the North American Sector

Weina Guan,[a,b] Xianan Jiang,[b,c] Xuejuan Ren,[a] Gang Chen,[d] and Qinghua Ding[e]

[a] *China Meteorological Administration–Nanjing University Joint Laboratory for Climate Prediction Studies, Institute for Climate and Global Change Research, School of Atmospheric Sciences, Nanjing University, Nanjing, China*
[b] *Joint Institute for Regional Earth System Science and Engineering, University of California, Los Angeles, California*
[c] *Jet Propulsion Laboratory, California Institute of Technology, Pasadena, California*
[d] *Department of Atmospheric and Oceanic Sciences, University of California, Los Angeles, California*
[e] *Department of Geography, and Earth Research Institute, University of California, Santa Barbara, California*

ABSTRACT: The leading interannual mode of winter surface air temperature over the North American (NA) sector, characterized by a "warm Arctic, cold continents" (WACC) pattern, exerts pronounced influences on NA weather and climate, while its underlying mechanisms remain elusive. In this study, the relative roles of surface boundary forcing versus internal atmospheric processes for the formation of the WACC pattern are quantitatively investigated using a combined analysis of observations and large-ensemble atmospheric global climate model simulations. Internal atmospheric variability is found to play an important role in shaping the year-to-year WACC variability, contributing to about half of the total variance. An anomalous SST pattern resembling the North Pacific mode is identified as a major surface boundary forcing pattern in driving the interannual WACC variability over the NA sector, with a minor contribution from sea ice variability over the Chukchi and Bering Seas. Findings from this study not only lead to improved understanding of underlying physics regulating the interannual WACC variability, but also provide important guidance for improved modeling and prediction of regional climate variability over NA and the Arctic region.

KEYWORDS: North America; Extratropical cyclones; Surface temperature; Interannual variability

1. Introduction

In contrast to the pronounced warming and rapid sea ice loss over the Arctic in recent decades, frequent occurrence of cold harsh winters has been observed over Eurasia and central North America (NA), jointly featuring a "warm Arctic, cold continents" (WACC) pattern (e.g., Overland et al. 2011; Cohen et al. 2014; Kug et al. 2015; Sun et al. 2016). A WACC pattern has also been identified as a prevailing interannual variability mode in surface air temperature (SAT) anomalies during boreal winter over the mid- to high latitudes of Eurasia and NA (Kug et al. 2015; Blackport et al. 2019; Mori et al. 2019a; Guan et al. 2020a; see Fig. 1a for an example of the WACC pattern over the NA sector). These cold extreme weather events over midlatitude continents and Arctic warm episodes are linked together via recurrent atmospheric anticyclonic circulation anomalies, and are sustained by the circulation-induced temperature and moisture advection and associated anomalous surface radiative and turbulent heat fluxes (e.g., Lee 2012; Sorokina et al. 2016; Park et al. 2015; Blackport et al. 2019). The origin of the anticyclonic circulation anomalies, which is the key to understanding the underlying physics in driving the interannual WACC pattern, however, remains unclear.

With a main focus on the interannual time scale, many studies have suggested that sea ice loss over the Barents–Kara Seas (BKS) and Chukchi–Bering Seas (CBS), respectively, associated with Arctic warm SAT anomalies, is crucial in exciting the anomalous anticyclonic circulation over the Eurasian and NA sectors via tropospheric or stratospheric planetary waves, and thus the WACC pattern, leading to enhanced Arctic warming (Inoue et al. 2012; Tang et al. 2013; Kug et al. 2015; Peings and Magnusdottir 2014; Semenov and Latif 2015; Orsolini et al. 2012; Nakamura et al. 2016; Xue et al. 2017; Zhang et al. 2018). Therefore, this represents a positive feedback in sustaining the WACC pattern. However, climate models exhibit diverse responses in midlatitude SAT anomalies to Arctic sea ice loss (e.g., Cohen et al. 2020). While most previous modeling studies focused on the Eurasian sector, cooling anomalies over midlatitude continents as a response to BKS sea ice loss on the interannual time scale are able to be simulated in several model simulations; the amplitudes of the cooling anomalies are generally much weaker than their observed counterparts (e.g., Mori et al. 2014; Kim et al. 2014; Mori et al. 2019a; Blackport et al. 2019). In contrast, close association between observed interannual BKS sea ice and midlatitude continental cooling anomalies over Eurasia could not be represented in several other modeling studies (e.g., Sun et al. 2016; Chen et al. 2016; McCusker et al. 2016; Ogawa et al. 2018). Rather limited modeling studies have been conducted to explore potential impacts of CBS sea ice on temperature anomalies over the NA continent.

On the other hand, previous studies indicated a possible role of tropical sea surface temperatures (SSTs) in driving the interannual WACC pattern. La Niña–like SST anomalies over
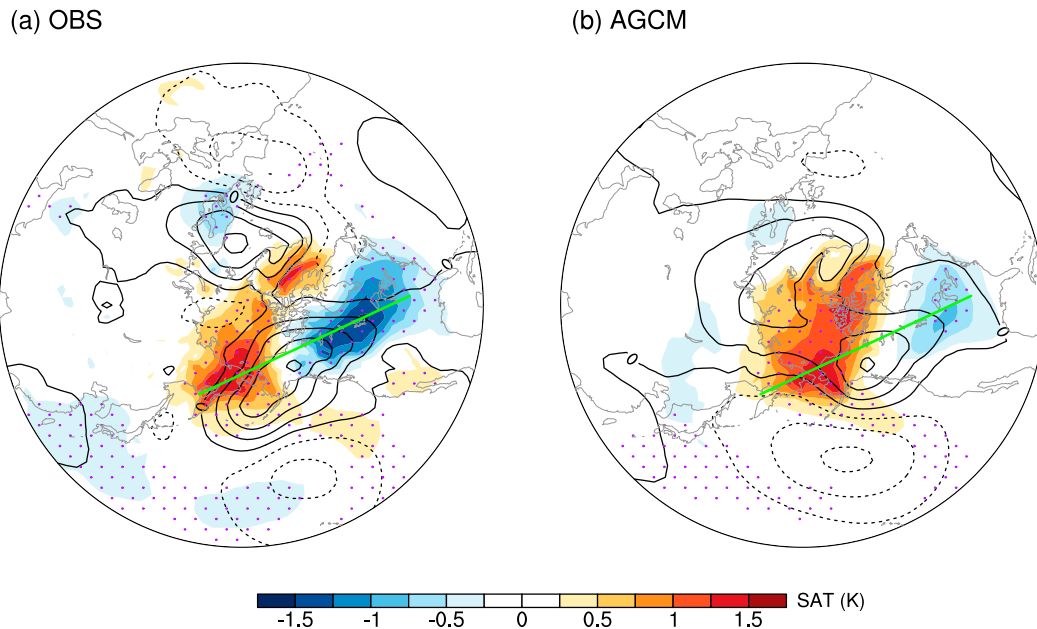
(a) OBS (b) AGCM

SAT (K)

FIG. 1. Winter SAT (shading; scaled by the color bar) and PS (contours; dashed when negative; interval: 0.5 hPa) anomalies in (a) observations and (b) AGCMs associated with the leading SVD mode of winter SAT anomalies between observations and simulations over 20°–90°N, 120°E–60°W, which are derived by regressing their anomalies onto the respective normalized expansion coefficients, i.e., EC$_{OBS}$ and EC$_{AGCM}$. Regressions based on simulations are calculated using the total 96 members of multimodel simulations, i.e., with a total combined time series of 3360 winters. The green lines, with the two end points of 35°N, 100°E and 90°N, 320°W, represent the axis linking the two SAT anomalous centers of the WACC pattern used for the cross sections shown in Fig. 3. Areas with stippled purple dots indicate the shaded anomalies surpassing the 95% significance level.

the tropical eastern Pacific (TEP) could induce a WACC-like pattern over the NA sector through Rossby wave trains across the North Pacific (NP; Clark and Lee 2019), and also possibly lead to cold winters over Eurasia via an indirect impact on tropical Atlantic SST and associated teleconnection patterns (Matsumura and Kosaka 2019). Pacific SST anomalies have also been proposed to play a role for the unexpected cold winters over central NA and accompanying drought over California during the winters of 2012–15 (e.g., Palmer 2014; Hartmann 2015; Seager et al. 2015; Lee et al. 2015; Wang et al. 2014; Watson et al. 2016), although there exists a debate on the relative importance of SST anomalies over the tropical Pacific versus extratropics over the NP (e.g., Hartmann 2015; Baxter and Nigam 2015; Teng and Branstator 2017).

In addition to these above remote or local boundary forcing by Arctic sea ice and SST anomalies, there is increasing evidence that the anomalous anticyclonic circulation that drives the interannual WACC pattern can also be ascribed to internal atmospheric variability (e.g., Sorokina et al. 2016; Gong and Luo 2017; Mori et al. 2019a; Blackport et al. 2019; Sigmond and Fyfe 2016; Sun et al. 2016; McCusker et al. 2016; Ogawa 2018). The internal variability of atmospheric circulation over the mid- to high latitudes of Eurasia and NA continents is often manifested by the vigorous subseasonal variability. For example, a similar WACC pattern in SAT anomalies has been recently reported as a leading *subseasonal* SAT variability mode to link Arctic sea ice changes and winter SAT anomalies over midlatitude

continents (e.g., Lin 2018; Guan et al. 2020b), representing a cross-scale influence on the interannual WACC variability (Sorokina et al. 2016; Guan et al. 2020a).

Considering the complex interplay of surface boundary forcing, including SST and sea ice, and internal atmospheric variability in possibly contributing to the formation of the WACC pattern, as well as the interactive feedback among land, ocean, and atmosphere, identification of the key processes responsible for the observed WACC variability remains challenging. Large-ensemble atmospheric-only global climate model (AGCM) simulations, forced by the observed SST and sea ice, can provide a useful tool to assess the relative contributions of boundary forcing versus atmospheric internal variability in generating the WACC pattern, although atmospheric influences on SST and sea ice variability are not resolved in these AGCM simulations. For example, by analyzing large-ensemble multimodel simulations, Mori et al. (2019a) found that in addition to internal atmospheric processes, BKS sea ice variability plays an important role in contributing to the interannual variability and long-term trend of the winter WACC pattern over the Eurasian sector, while the role of the SST anomalies is largely negligible.

As the interannual WACC variabilities over the Eurasian and NA sectors are not necessarily related to each other (e.g., Kug et al. 2015), and also considering that insufficient attention has been given to understanding the causes of the WACC variability over the NA sector, in this study we have conducted

TABLE 1. Descriptions of the AGCM experiments in the NOAA FACTS. See the FACTS project website for more details: https://www.psl.noaa.gov/repository/a/factsdocs.

		Forcings		
Expt name	Description	SST	Sea ice	Greenhouse gases and ozone
amip_obs_rf	AMIP with observed radiative forcing	Obs	Obs	Obs
amip_clim_polar	AMIP with observed radiative forcing, climatological sea ice, and polar SST	Obs/present climatology	Present climatology	Obs
eof1_sst	The first leading EOF mode of global SST variability with observed radiative forcing	First EOF	Obs	Obs

an analysis to quantitatively characterize the relative importance of surface boundary forcing versus internal atmospheric processes in regulating the interannual WACC variability over the NA sector. The outcome of this study is expected to improve our understanding and modeling/prediction capability of the NA regional climate variability on the interannual time scales. Hereafter, the NA sector is referred to an extended region including eastern Siberia, the NA continent, and the neighboring NP and Arctic regions. The remainder of this paper is organized as follows. Section 2 introduces the observation and multimodel datasets used in this study, and the approach to extract the leading interannual WACC mode over the NA sector by employing a combined analysis of observations and AGCM simulations following Mori et al. (2019a). Section 3 presents main results on quantitative characterization of critical processes responsible for the interannual WACC variability over the NA sector based on both observations and multimodel simulations. A summary and brief discussion are given in section 4.

2. Data and method

a. Observation and model datasets

Monthly observational data used in this study include SAT, surface pressure (PS), 3D geopotential height (Z), zonal and meridional winds (u, v), and temperature (T) from ERA-Interim (Dee et al. 2011), and sea ice concentration (SIC) and SST from the Met Office Hadley Centre (Rayner et al. 2003) for the period of 1979–2013.

The same monthly variables except SIC and SST from climate model simulations based on AGCMs participated in the NOAA Facility for Climate Assessments (FACTS; Murray et al. 2020) are also analyzed in this study. These large-ensemble Atmospheric Model Intercomparison Project (AMIP; Gates et al. 1999)-type AGCM simulations are particularly useful for assessment of predictable signal and comparing that to the climate system's internal variability (Sun et al. 2016, 2018; Mori et al. 2019a; Murray et al. 2020). Analyses in this study mainly focus on simulations from the amip_obs_rf experiment from FACTS, in which the eight AGCMs are forced by the observed monthly mean boundary layer conditions including SST and sea ice, and historical changes in natural and anthropogenic radiative forcing and aerosol emissions (see Tables 1 and 2 for details of FACTS experiments and models). Available simulations from three of the eight AGCMs participated in the amip_clim_polar and eof1_sst experiments are also analyzed. While the observed historical radiative forcing specified in the latter two experiments is the same as in the amip_obs_rf, climatological sea ice along with climatological SST over the grids where climatological sea ice is present are specified in the amip_clim_polar experiment to isolate the role of extrapolar SST variability for model atmospheric variability; in contrast, SST anomalies of the leading empirical orthogonal function (EOF) mode of the observed monthly mean SST variability (refer to Fig. 9a), which largely represents SST variability associated with the El Niño, are used as the boundary forcing in the experiment eof1_sst along with the observed monthly sea ice (see Table 1 for more details). If not specially mentioned, model results in the following discussions are based on the amip_obs_rf experiment.

TABLE 2. Description of FACTS AGCMs analyzed in this study. Note that while simulations from all the eight AGCMs are available from the amip_obs_rf experiment, only the three AGCMs marked with an asterisk (*) are available for both the amip_clim_polar and eof1_sst experiments.

Model name	Institute	Ensemble size	Horizontal resolution (lon × lat)
AM3	Geophysical Fluid Dynamics Laboratory (GFDL)	17	1.9° × 1.9°
CAM4*	National Center for Atmospheric Research (NCAR)	20	1° × 1°
ECHAM5*	Max Planck Institute for Meteorology (MPI)	50	0.75° × 0.75°
ESRL-CAM5	National Center for Atmospheric Research (NCAR)	40	1° × 1°
ESRL-CAM5L46	National Center for Atmospheric Research (NCAR)	16	1° × 1°
ESRL-GFSv2*	NOAA/NWS Environmental Modeling Center (EMC)	50	1° × 1°
GEOS-5	NASA Goddard Space Flight Center (GSFC)	12	1.25° × 1°
LBNL-CAM5	National Center for Atmospheric Research (NCAR)	50	1° × 1°

Both the reanalysis and model data are interpolated onto common 2.5° × 2.5° grids. To focus on the interannual WACC variability, winter mean (November–March)[1] anomalies of various fields from both observations and simulations were derived by removing climatological mean and linear trends. Climatology of these variables is separately derived for observations and each ensemble simulation from the eight AGCMs by averaging over the 35 winters from 1979 to 2013.

b. Analysis methods

Considering the model deficiencies in representing the WACC pattern over the NA sector (to be discussed more later), a combined analysis method using both observations and multimodel large-ensemble simulations (e.g., Benestad et al. 2017; Mori et al. 2019a) is adopted to extract a leading interannual WACC pattern in model simulations similar to the observed counterpart. As in Mori et al. (2019a), the leading interannual SAT variability mode in observations and model simulations over the NA sector is derived by a singular value decomposition (SVD) analysis of the combined winter SAT anomalies from observation and simulations. In the SVD analysis, the spatial structures of the observed and simulated leading modes of winter SAT anomalies are determined in such a way that the modes explain the maximum squared temporal covariance between observations and simulations over the analysis domain (e.g., Bretherton et al. 1992). In the FACTS experiment amip_obs_rf, as the boundary and radiative forcing specified in each member of the AGCM simulations is exactly the same following the observed historical SST and sea ice anomalies, this SVD analysis method is expected to derive a leading interannual SAT mode over the NA sector in model simulations as close as possible to the observed leading SAT pattern.

The SVD analysis is conducted based on the covariance matrix of the combined observed and simulated winter SAT anomalies over the domain 20°–90°N, 120°E–60°W (~2117 spatial points). Considering a minimum ensemble size of 12 available in all the eight AGCMs, only 12 members from each model are used for the SVD analysis (i.e., a total of 96 members), although the remaining members will also be included for other analyses to make full use of large model ensembles. The SVD analysis is performed between one set of 35-winter model anomalous SAT data with all 96 members combined together and another set of the observed SAT data, which duplicates the observed 35-winter record 96 times to match the model data length (i.e., with a time series of total 3360 winters on 2117 spatial points for both observational and model data). The derived singular vectors based on the SVD analysis depict the leading spatial patterns of the interannual SAT variability modes in observations and simulations, and the associated expansion coefficients (ECs) contain the corresponding time series during the 35-winter period for the observations (also duplicates 96 times) and simulations in each model member. In the following discussions, ECs for both observations and

simulations are normalized over the 3360 temporal points so that their corresponding amplitude of SAT variability can be directly compared based on their leading SVD patterns. The statistical significance of temporal correlations between observations and simulations during the 35 winters is calculated based on the two-sided Student's t test with the effective degree of freedom of the time series estimated by the lag-1 autocorrelation following Bretherton et al. (1999).

3. Results

a. The leading WACC pattern based on the combined analysis of observation and model data

Figures 1a and 1b show patterns of the leading covariability mode of winter SAT anomalies and associated anomalous surface pressure (PS) in observations and models based on the SVD analysis, derived by regressions of SAT and PS anomalies against the normalized ECs (i.e., EC_{OBS} and EC_{AGCM}). For model simulations, regressions are calculated using the total 96 members of multimodel simulations, while regressions for observations are based on one 35-winter period due to duplicated observational data when performing the SVD analysis. The observed and simulated SAT anomalies of the leading SVD mode, which explains 40% of the total squared covariance of the observed and simulated SAT variations, capture the WACC pattern over the NA sector—that is, warm anomalies centered over eastern Siberia (ES)/Alaska and cold anomalies over central NA—along with the anomalous Alaskan high in bridging the two anomalous SAT centers. As previously mentioned, the anomalous anticyclonic circulation is expected to sustain the WACC pattern by advecting cold air from the Arctic into central NA, and warm and moist air from the south into the CBS (e.g., Kug et al. 2015; Guan et al. 2020a). While the warming anomalies over the Arctic are well simulated, the amplitude of cold anomalies over central NA is significantly underestimated in models by about 50% (Fig. 1b). Anomalous PS distribution associated with the WACC pattern as illustrated in Fig. 1 bears a strong resemblance to the North Pacific Oscillation (NPO)/west Pacific (WP) teleconnection pattern, a dominant mode of the midlatitude atmosphere over the NP (e.g., Feldstein 2000; Linkin and Nigam 2008; Tanaka et al. 2016; Baxter and Nigam 2015; Dai and Tan 2019), and the pattern associated with the so-called Alaskan ridge regime (Casola and Wallace 2007; Straus et al. 2007; Carrera et al. 2004).

Notably, there have been recent debates on the approach to extract the externally forced WACC variability using the SVD approach (Mori et al. 2021; Zappa et al. 2021). Zappa et al. (2021) suggested that rather than homogenous regressions as used in Mori et al. (2019a) and also in this study, heterogeneous regressions need to be applied to examine the covarying WACC patterns between the observations and AGCM simulations. It is found that the WACC patterns in both observations and AGCM simulations based on homogenous regressions as shown in Fig. 1 are very close to those derived based on heterogeneous regressions (figure not shown), as shown in Mori et al. (2021). Also note that a very similar WACC pattern as shown in Fig. 1a can be obtained as the first

---

[1] The 1979 winter represents the period from 1 November 1979 to 31 March 1980, and so on.
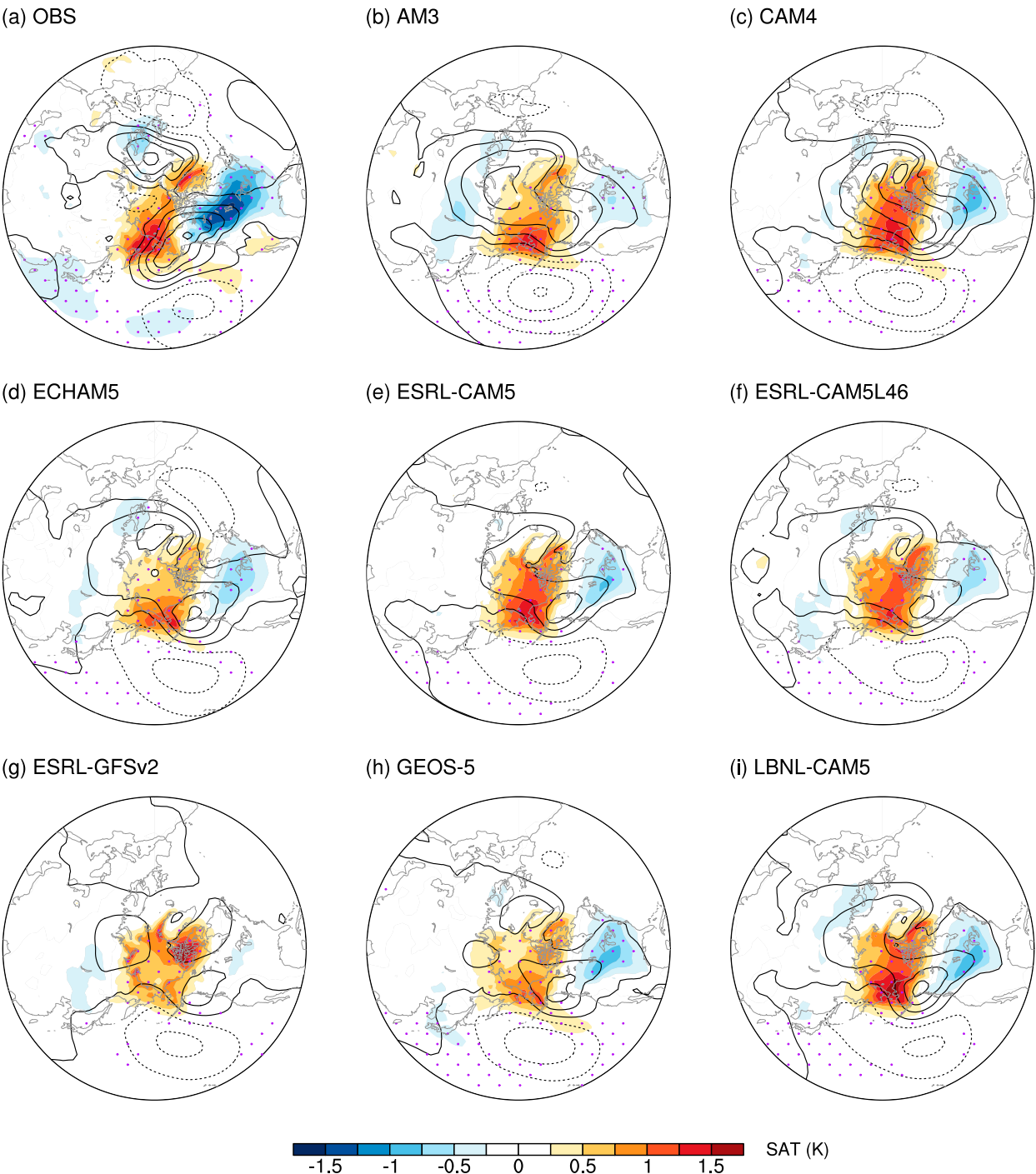
SAT and SLP anomalies regresssed on ECs

FIG. 2. As in Fig. 1, but for SAT (shading) and PS (contours) anomalies in (a) observations (duplicated from Fig. 1a) and (b)–(i) simulations based on individual models.

leading EOF mode of the observed 35-winter SAT anomalies over the same region.

Anomalous SAT and PS patterns in individual models associated with the leading SVD mode are illustrated in Fig. 2 by

applying a similar regression approach but only using the ECs corresponding to the 12 members of that model. Again, while the Arctic warming anomalies are generally well simulated in all these AGCMs, the observed cold anomalies over central
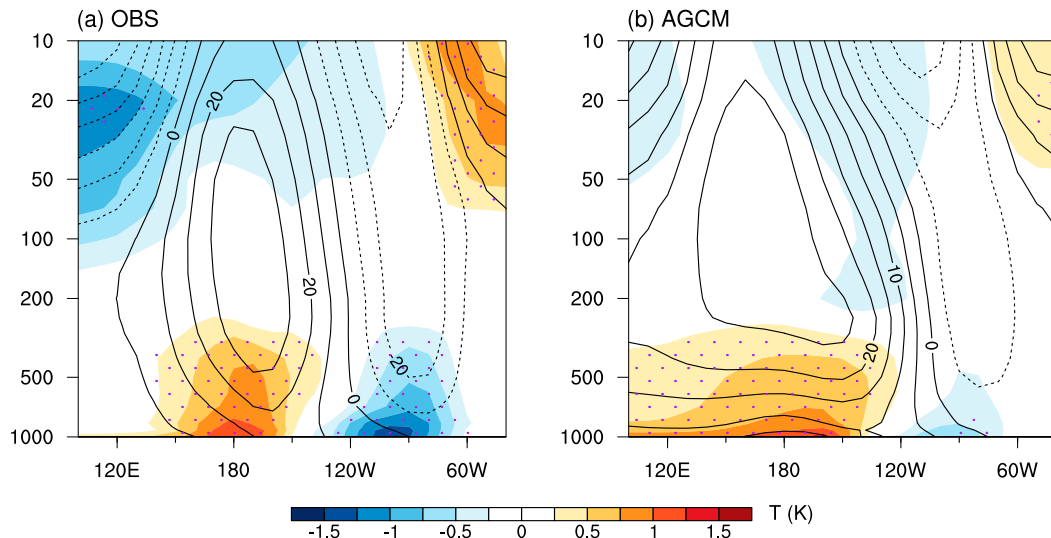
FIG. 3. Longitude–height cross sections of T (shading) and Z (contours; dashed when negative) anomalies associated the WACC pattern in (a) observations and (b) simulations. These anomalies are derived by regressions onto normalized EC_{OBS} and EC_{AGCM} and averaged over a $10°$ latitude band ($5°$ north and south) along the green lines in Fig. 1. As in Fig. 1, regressions based on models are calculated using the total 96 members of multimodel simulations.

NA are significantly underestimated in model simulations, along with a largely weakened anticyclonic anomalies near Alaska. Particularly note that cold anomalies over central NA and anomalous Alaskan high associated with the leading SVD mode are largely absent in simulations from ESRL-GFSv2 (Fig. 2g). This will be further discussed in the following.

Vertical–horizontal cross sections of temperature and geopotential height anomalies in both observations and model simulations associated with the leading SVD mode along the axis linking the two anomalous SAT centers in the WACC pattern (i.e., the green lines in Fig. 1) are further illustrated in Fig. 3. Both observations and simulations suggest that SAT anomalies associated with the WACC pattern are connected to air temperature anomalies in a deep tropospheric layer up to about 300 hPa; meanwhile, the anomalous surface high near Alaska is closely linked to equivalent-barotropic ridge anomalies vertically extending into the stratosphere (Figs. 3a,b). This indicates that the WACC pattern is not likely a direct response to the local surface boundary forcing; rather, it is driven by circulation associated with large-scale tropospheric and stratospheric waves as previously proposed (e.g., Blackport et al. 2019).

b. Optimal boundary conditions in forcing the interannual WACC variability

Figure 4 presents the time series of the ECs for each member of the eight AGCMs (gray lines) along with the ensemble-mean EC over all 96 model members (blue line; hereafter $\overline{EC}_{AGCM}$) and EC based on the observations (red line; EC_{OBS}) during the 35 winters. Pronounced internal atmospheric variability associated with the WACC pattern is readily seen by the spread of the ECs among individual model members. Considering that the impact of internal atmospheric variability is largely averaged out by the large-ensemble mean,

the $\overline{EC}_{AGCM}$ therefore represents the forced WACC variability due to boundary forcing, including SST and sea ice. As $\overline{EC}_{AGCM}$ is highly correlated with EC_{OBS} ($r = 0.73$), this suggests that a considerable portion (~50%) of the observed WACC variability can be ascribed to the SST and sea ice variability specified as the boundary forcing in AGCMs.

Following Mori et al. (2019a), the prevailing SAT patterns associated with the internal atmospheric variability can be derived by an EOF analysis of intra-ensemble SAT anomalies over the NA sector ($20°$–$90°N$, $120°E$–$60°W$) based on model simulations. Intra-ensemble SAT anomalies are defined as the deviations of detrended winter SAT anomalies from ensemble-mean fields across model simulations (i.e., by removing the forced WACC variability). While the first leading mode of internal SAT variability exhibits a Pacific–North America (PNA)-like pattern, a similar WACC pattern in SAT anomalies to that shown in Fig. 1a is identified as the second leading
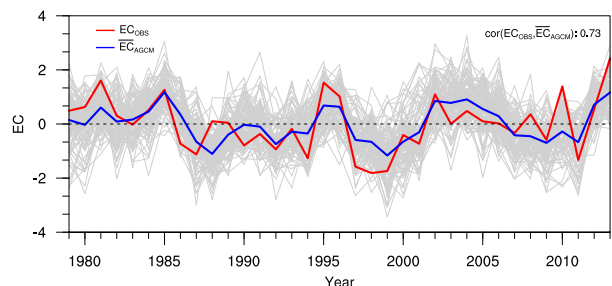

FIG. 4. The normalized EC time series for the observations (EC_{OBS}; red), and AGCM simulations for individual members (gray) along with the mean averaged over 96 ensemble members ($\overline{EC}_{AGCM}$; blue).
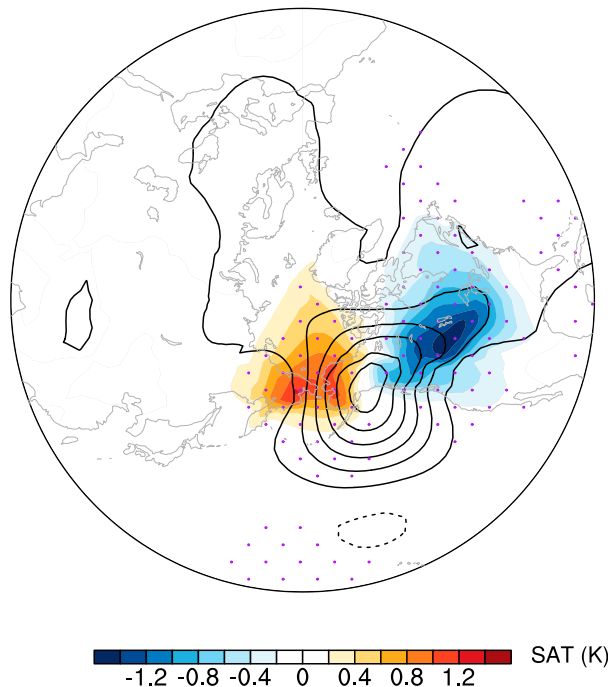
FIG. 5. The second leading internal SAT variability mode (shading; dotted areas for 95% significance level) and associated PS (contours; dashed if negative; interval: 0.4 hPa) anomalies based on multimodel simulations as derived by an EOF analysis of intra-ensemble SAT anomalies over 20°–90°N, 120°E–60°W. Intra-ensemble SAT anomalies are defined as the deviations of detrended winter SAT anomalies from ensemble-mean fields across model simulations. SAT and PS anomalies shown here are obtained by regressions onto the principal component (PC) of the EOF2 of the internal SAT variability mode. The first EOF mode is associated with El Niño.
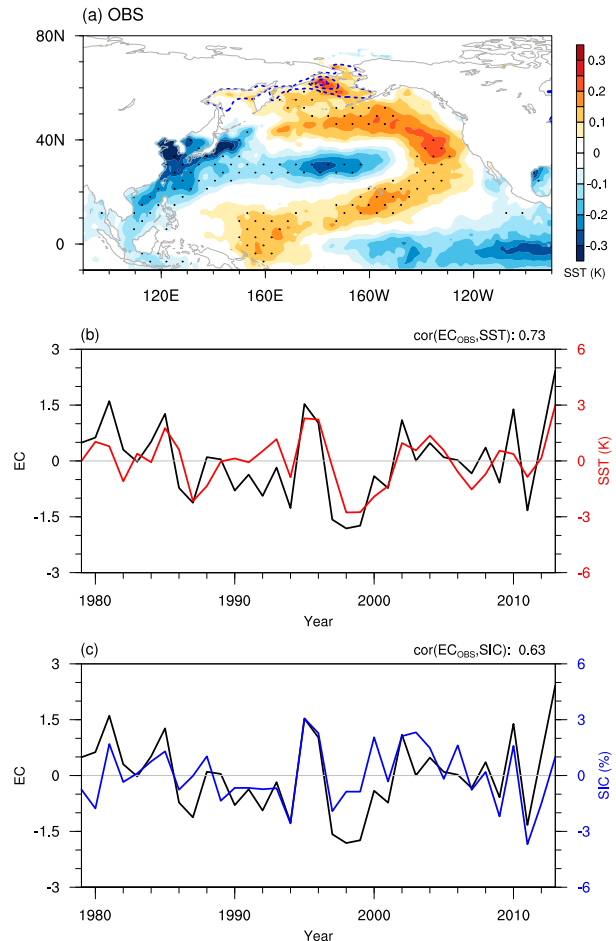

FIG. 6. (a) Regression patterns of SST (shading; dotted areas for 95% statistical significance level) and SIC (contours; dashed when negative; interval: 2%) anomalies onto EC$_{OBS}$. (b),(c) Time series of SST (red) and SIC (blue) indices along with EC$_{OBS}$ (black). The SST and SIC indices series are calculated by projecting winter SST anomalies over 10°–65°N, 120°E–120°W and SIC anomalies over 50°–75°N, 140°E–160°W onto their corresponding patterns in (a). Note that the signal of the SIC index is reversed so that a positive SIC index corresponds to reduced SIC over CBS.

mode (Fig. 5), indicating that the WACC pattern is an intrinsic SAT variability mode over the NA sector.

Key regions of SST and sea ice anomalies responsible for the observed and forced WACC variability can further be identified by the regression patterns of SST and sea ice anomalies against the time series of EC$_{OBS}$ and $\overline{EC}_{AGCM}$ during the 35 winters, respectively. Figure 6a presents regressed anomalous SST (shading) and sea ice (contours) associated with the observed WACC variability. The observed WACC pattern is closely linked to sea ice loss over CBS as previously reported (e.g., Kug et al. 2015; Blackport et al. 2019; Guan et al. 2020a), although the causality is difficult to be determined based on the observations due to the two-way interactions between Arctic sea ice and atmosphere. The WACC pattern over the NA sector is also found to be associated with negative SST anomalies over the central and western NP along 40°N and surrounding positive anomalies over the eastern part of the NP basin and CBS, as well as a small patch of warm SST anomalies over the tropical western Pacific (TWP) near 160°E. Although La Niña–like negative SST anomalies over TEP are also discerned associated with the observed WACC variability, they are not statistically significant (Fig. 6a).

Figure 7a similarly illustrates anomalous SST and sea ice patterns associated with the forced WACC variability in AGCM simulations by regressing these fields onto model ensemble mean EC (i.e., $\overline{EC}_{AGCM}$) during the 35 winters. As in the observations, the forced WACC pattern is also closely associated with sea ice loss over the CBS region, along with negative SST anomalies over the central NP near 40°N and surrounding horseshoe-like shaped positive SST anomalies over the eastern part of the NP basin and TWP near 160°E (Fig. 7a). Note that the La Niña–type negative SST anomalies over TEP associated with the WACC variability in the observations are not evident in model simulations (cf. Figs. 6a and 7a), suggesting that the SST variability over TEP associated with El Niño/La Niña may not play a crucial role in driving the forced WACC pattern. This is further supported by the
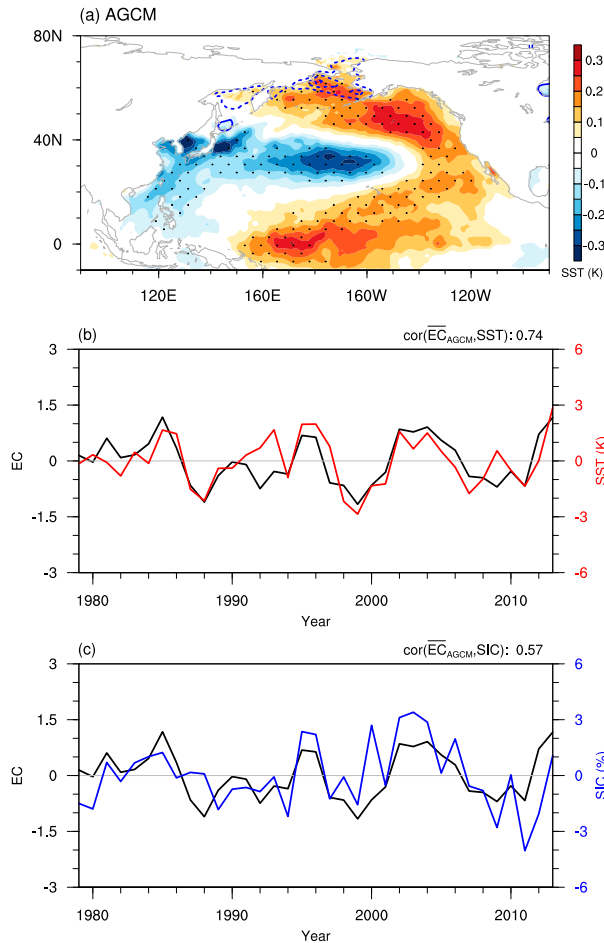
FIG. 7. As in Fig. 6, but for (a) regression patterns of SST and SIC anomalies onto $\overline{\mathrm{EC}}_{\mathrm{AGCM}}$ and (b),(c) time series of SST, SIC, and $\overline{\mathrm{EC}}_{\mathrm{AGCM}}$ based on model simulations. Note that the SST and SIC time series are different between Figs. 6b,c and 7b,c, although highly correlated, due to slight differences in the regression patterns between observations (Fig. 6a) and models (Fig. 7a). Also see details in the text.

similarly regressed anomalous SST and sea ice patterns but corresponding to the forced WACC variability based on 12-member ensemble mean in each model (Fig. 8). While regressed SST anomalies over the TEP are not statistically significant in most of these AGCM simulations, the La Niña–type negative SST anomalies over the TEP associated with the forced WACC variability as in the observations is found in three of the eight models (i.e., ECHAM5, ESRL-GFSv2, and GEOS-5); in contrast, strong El Niño–type SST anomalies over the TEP is found in several other AGCMs, including AM3, CAM4, ESRL-CAM5, and LBNL-CAM5 (Fig. 8).

The interannual SST and sea ice indices closely associated with the WACC variability can be derived by projecting the observed winter SST and sea ice anomalies onto their corresponding regressed anomalous patterns over respective key regions identified in Figs. 6a and 7a: the CBS region (50°–75°N, 140°E–160°W) for sea ice, and the NP (10°–65°N, 120°E–120°W)

for SST.[2] These projections are conducted independently for observations and model simulations due to their slight differences in the corresponding regression patterns as shown in Figs. 6a and 7a. The derived SST and sea ice indices associated with the observed and simulated WACC variability are presented in Figs. 6b,c and 7b,c, respectively. Consistent with the regressed SST and sea ice patterns in Figs. 6a and 7a, both the time series of the observed (EC$_{\mathrm{OBS}}$) and forced WACC variability in models ($\overline{\mathrm{EC}}_{\mathrm{AGCM}}$) during the 35 winters are strongly correlated with CBS sea ice index ($r = 0.63$ and 0.57, respectively; see Figs. 6c and 7c) and SST over the NP ($r = 0.73$ and 0.74, respectively; Figs. 6b and 7b). Note that similar correlations can be obtained if the same SST and sea ice indices are used for observations and models by projections onto regressed anomalous SST and sea ice patterns from either observations or simulations (not shown).

Since the observed SST and sea ice are specified in AGCM simulations and do not respond to atmospheric variability, the close association between the forced WACC variability and the derived SST/sea ice indices as shown in Fig. 7 indicates important roles of sea ice and SST anomalies in driving the WACC variability. In addition to CBS sea ice loss as previously reported, these results indicate that the anomalous SST variability over the NP also plays a critical role for the formation of the WACC pattern over the NA sector. Of particular interest, this anomalous SST pattern, especially that based on the observations in Fig. 6a, is reminiscent of the North Pacific Mode (NPM; Deser and Blackmon 1995; Park et al. 2012; Hartmann 2015; Peng et al. 2018a), which emerges as the second leading mode of the observed interannual SST variability over the NP basin (Fig. 9b) following the first leading mode that is closely linked to El Niño/La Niña (Fig. 9a). While the NPM is independent from El Niño, a positive phase of the NPM as shown in Fig. 9b is often observed prior to an El Niño winter, a so-called seasonal fingerprinting mechanism to set the stage for El Niño via tropical–extratropical interactions (e.g., Vimont et al. 2003; Wang et al. 2014).

Figure 9d further illustrates that SAT anomalies associated with the NPM indeed exhibit a WACC pattern over the NA sector along with surface anticyclonic circulation anomalies near Alaska, showing a strong resemblance of the observed WACC pattern in Fig. 1a. The surface high anomalies near Alaska associated with the NPM (Fig. 9d) are also linked to vertically extended equivalent-barotropic high anomalies (figure not shown, but similar to what is shown in Fig. 3), which tends to be sustained by strong northward wave fluxes in the lower troposphere from the central NP (Fig. 9d). Largely similar SAT and PS anomalous patterns associated with the NPM are also found in multimodel simulations (figure not shown). In contrast, SAT anomalies over the NA sector associated with El Niño/La Niña are less well organized and much weaker than those associated with the NPM (Fig. 9c). These results lend further support of a crucial role of the NPM-like SST variability in driving the WACC pattern as suggested in

---

[2] Slight changes of these domains, for example, by including TWP for the SST projections, will lead to largely similar results.
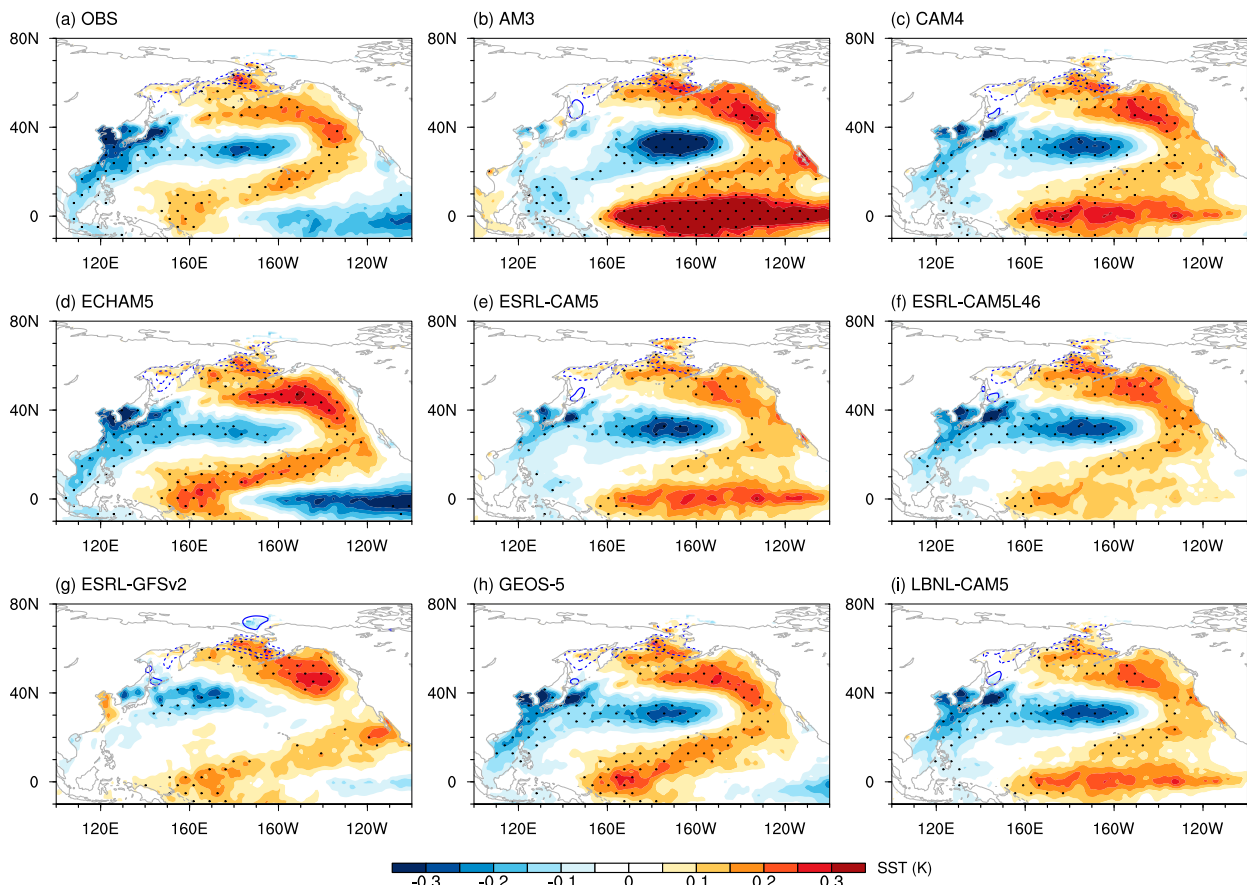
FIG. 8. (b)–(i) As in Figs. 6a and 7a, but for regressed SST and SIC patterns based on individual model simulations. Also shown is (a) the observational counterpart, duplicated from Fig. 6a.

Figs. 6 and 7, while El Niño/La Niña may not be critical in sustaining the WACC variability over the NA sector. An important role of the NPM-like anomalous SST pattern underlying the extremely cold anomalies over central NA and Californian drought during the 2013/14 winter has also been widely reported (e.g., Baxter and Nigam 2015; Hartmann 2015; Wang et al. 2014; Seager et al. 2015; Lee et al. 2015).

To further quantify the relative roles of SST variability associated with the El Niño/La Niña (i.e., EOF_1 in Fig. 9a) and the NPM (EOF_2 in Fig. 9b) for the observed WACC variability, Fig. 10 shows time series of WACC indices during the 35 winters explained by EOF_1, EOF_2, and EOF_1 and EOF_2 together, respectively. The WACC coefficient associated with each EOF mode in a particular winter is derived by projecting its related SAT anomalous pattern, constructed by the corresponding regressed anomalous SAT distribution (i.e., Figs. 9c,d) weighted by the principal component of the EOF mode, onto the observed WACC pattern in Fig. 1a. Correlations between the observed WACC variability (e.g., EC_{OBS}) and the WACC indices associated with EOF_1, EOF_2, and both EOF_1 and EOF_2 are 0.11, 0.57, and 0.57 (Fig. 10), respectively, confirming that SST variability associated with the NPM plays a more important role in contributing to the observed WACC variability than that associated with El Niño/La Niña. In addition to a very weak

correlation to the EC_{OBS}, El Niño/La Niña–related WACC variability exhibits a very weak amplitude (Fig. 10a). Note that a much higher correlation (~0.8) between EC_{OBS} and the NPM related WACC index is found after 1995, in contrast to a poor correlation during a short period around 1990 (e.g., 1988–93; Fig. 10b). A very weak correlation between EC_{OBS} and $\overline{EC}_{AGCM}$ is also noted around 1990 (Fig. 4), suggesting a more chaotic nature of atmospheric variability during this period for a reason that needs to be further understood.

A minor role of SST variability associated with the El Niño/La Niña for the observed WACC variability over the NA sector is further confirmed by a weak correlation (0.22) between the time series of the observed WACC variability (EC_{OBS}) and the ensemble-mean WACC indices based on three FACTS AGCM simulations in the eof1-sst experiment (Fig. 11c), in which only the observed monthly SST anomalies associated with El Niño/La Niña are specified along with observed sea ice and radiative forcing (see Table 1).

c. Relative role of internal processes versus SST and sea ice forcing for the WACC variability

Relative importance of internal atmospheric variability versus surface boundary forcing in driving the interannual WACC variability over the NA sector is further investigated.
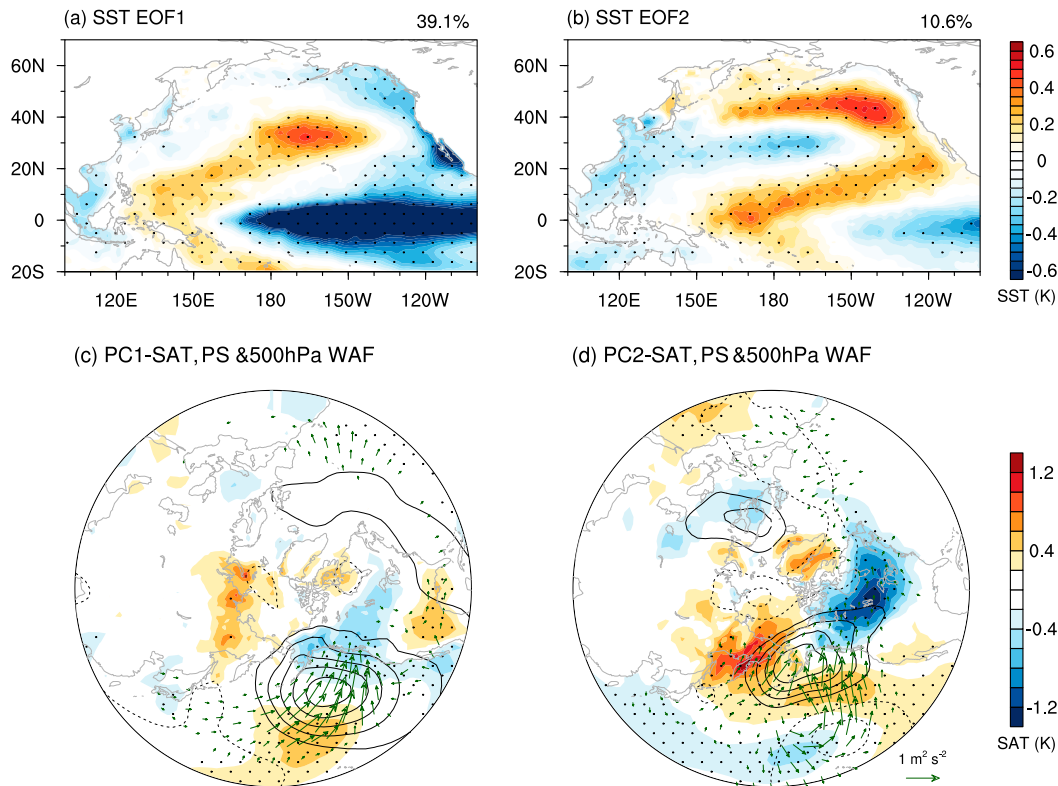
FIG. 9. Spatial patterns of SST anomalies associated with the (a) first and (b) second EOF modes of the observed winter SST anomalies over 30°S–65°N, 120°E–105°W from 1979 to 2013, derived by regressing winter SST anomalies onto the normalized PC$_1$ and PC$_2$ of the two leading interannual SST mode. (c),(d) Regressed anomalous SAT (shading; dotted areas for 95% significance level) and PS (contours; dashed when negative; interval: 0.5 hPa) onto the normalized PCs, and associated wave activity flux (WAF) at 500 hPa (vectors; plotted only where WAFs are greater than 0.1 m^2 s^{-2}). The 2D WAF is calculated based on similarly regressed streamfunction anomalies following Takaya and Nakamura (2001). All variables in this figure are based on observations.

Following the approach by Mori et al. (2019a), the total WACC variance in observations and each of the eight AGCMs is estimated by the variance of their ECs corresponding to the leading SVD mode during the 35 winters, which contains effects from both surface boundary forcing and internal atmospheric variability. Calculations of the total WACC variance in each model are based on ECs across model members. Note that although only 12 ensemble members from each model were used for the SVD analysis, to make full use of the large model ensembles all available members are used for calculation of the total variance with their ECs during the 35 winters derived by projecting the winter SAT anomalies onto the singular vector of the model WACC pattern (i.e., Fig. 1b). As shown in Fig. 12 (yellow bars), while four models capture the total WACC variance comparable to the observations, the variance is significantly underestimated in other four models, consistent with their relatively weaker SAT amplitude in the WACC pattern, particularly the cold anomalies over central NA (see Figs. 1b and 2). The forced WACC variance in each model can then be further estimated by the variance of its corresponding ensemble mean EC during the 35 winters averaged over all available members, and are denoted by red

squares in Fig. 12. Difference between the total (yellow bar) and the forced variance (red square) for each model depicts contribution from atmospheric internal processes, which shows a range of 40%–60% of the total variance across these models. While this result is largely consistent with previous studies that suggested an important role of internal processes in regulating the WACC variability over the NA sector (e.g., Sigmond and Fyfe 2016; Peng et al. 2018b; Sun et al. 2016), it is the first time that a quantitative estimate of the contribution of the atmospheric internal processes to the total WACC variability over the NA sector is derived in this study.

The percentages of the total WACC variance explained by CBS sea ice and NP SST variability can be further estimated from correlations (r) between the previously defined sea ice (Figs. 6c and 7c)/SST indices (Figs. 6b and 7b) and ECs during the 35 winters in observations and model simulations across all available members (concatenated in time series) based on the coefficients of determination (r^2) approach. Figure 12 suggests that CBS sea ice (gray bars) plays a minor role in driving the WACC variability compared to SST anomalies over the NP basin (blue bars) in seven out of the eight models. In contrast to previous findings on the dominant role of BKS sea ice in
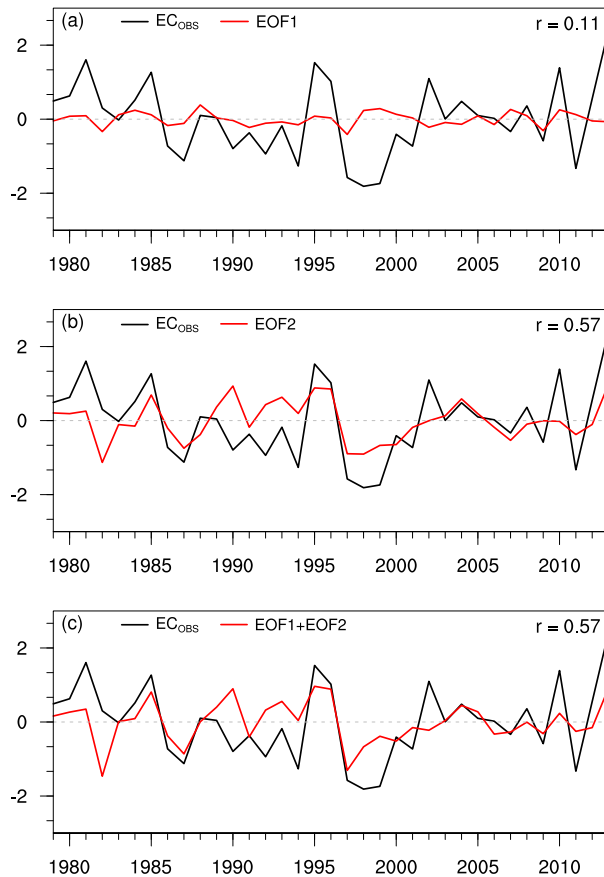
FIG. 10. Time series of the observed WACC variability (EC$_{OBS}$; black; duplicated from Fig. 4) and the WACC time series associated with the two leading SST modes in Fig. 9: (a) EOF$_1$ (El Niño/La Niña), (b) EOF$_2$ (NPM), and (c) EOF$_1$ + EOF$_2$. The WACC coefficient associated with each EOF mode is derived by projecting its related SAT anomalous pattern, constructed by the regressed anomalous SAT distribution (Fig. 9) weighted by the PC of the EOF mode in each winter, onto SAT anomalies of the observed WACC pattern over 20°–90°N, 120°E–60°W in Fig. 1a.

FIG. 11. (a) As in Fig. 4, but with model results only based on 36 members from three AGCMs (CAM4, ECHAM5, and ESRL-GFSv2). (b),(c) As in (a), but for model results based on the FACTS experiment amip_clim_polar and eof1_sst, respectively. ECs for each model member during the 35 winters in the amip_clim_polar and eof1_sst experiments are derived by projecting the winter SAT anomalies onto the singular vector of the model WACC pattern (i.e., Fig. 1b).

driving the WACC pattern over Eurasia (e.g., Mori et al. 2019a), on average only about 10% of the total WACC variance over the NA sector is explained by the interannual CBS sea ice variability; in contrast, about 22% of total WACC variability over the NA sector can be attributed to the NPM-like SST variability. An exception is found in ESRL-GFSv2, in which the sea ice effect dominates over that by SST anomalies. As previously discussed in Fig. 2, this model is also marked as an outliner with cold anomalies over central NA in the WACC pattern largely absent. Although further investigations are needed for complete understanding of the deficiencies in representing the WACC pattern in ESRL-GFSv2, this could be related to model insensitivity in responding to anomalous SST forcing, as indicated by the largely statistically insignificant SST signals over the NP associated with the forced WACC variability in this model (Fig. 8g). As a result, the large-scale Alaskan high anomalies and thus the cold anomalies over
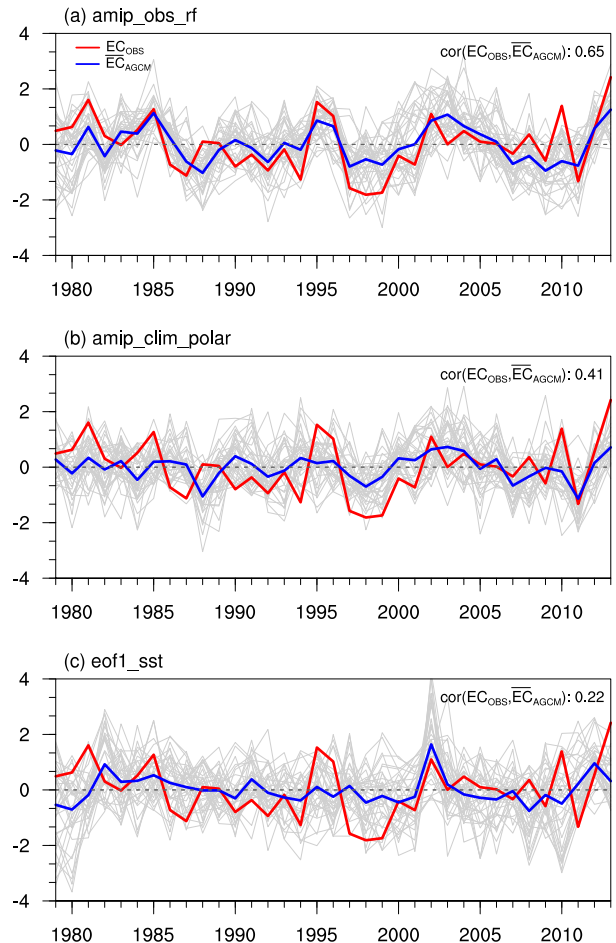
central NA cannot be effectively established, leading to largely regionally confined warming anomalies over the Arctic region induced by local sea ice variability (Fig. 2g).

Since sea ice loss over CBS associated with the WACC pattern is coincident with local warm SST anomalies (see Figs. 6a and 7a), the impact of CBS sea ice loss on the WACC variability as indicated by the r^2 approach in Fig. 12 could be partially included in that related to SST variability. The WACC variance explained by a combination of CBS sea ice and NPM-like SST variability is further estimated using a multiple linear regression of the sea ice and SST indices onto ECs, which is denoted by each green dot in Fig. 12. It is illustrated that the r^2 of WACC variance explained by a combination of SST and sea ice indices is only slightly higher than that by SST or sea ice alone, rather than a linear addition, confirming that influences of CBS sea ice and SST variability
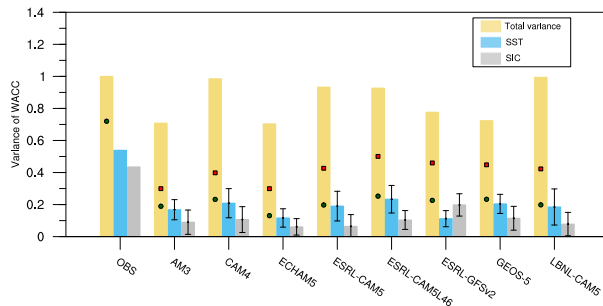
FIG. 12. Total WACC variance in observations and eight AGCMs (yellow bars, scaled by variance in observations). The red squares indicate total forced WACC variance, calculated based on the ensemble-mean EC_{AGCM} from each model. WACC variances explained by NP SST (blue bars) and CBS sea ice (gray bars) are estimated by r^2 between ECs in observations or simulations from all available members and the SST/SIC indices (error bars represent one standard deviation of explained variances across ensemble members). Variances explained by a combination of NP SST and CBS sea ice anomalies are denoted by dark green dots. See text for more details.

on the WACC pattern are not exclusive from each other. The lower values corresponding to green dots than those to red squares in Fig. 12 generally indicate that factors other than the combination of CBS sea ice and NP SST indices also contribute to the forced WACC variability in the model.

The relative role of sea ice and SST variability in driving the WACC variability is further examined by the FACTS experiment amip_clim_polar with simulations from three AGCMs. In this experiments, AGCMs are forced by climatological sea ice and polar SST where climatological sea ice is present, so that the forced model variability is largely ascribed to the observed SST variations over the extrapolar region (60°S–60°N). Note that the correlation between the observed WACC variability (EC_{OBS}) and the forced WACC variability ($\overline{EC}_{AGCM}$) based on these three AGCM simulations is slightly smaller than that using all eight GCMs [0.65 in the former (Fig. 11a) vs 0.73 in the latter (Fig. 4)], possibly due to less total model ensemble members to sufficiently suppress the internal variability when only using three GCMs. In the experiment amip_clim_polar (Fig. 11b), a correlation of 0.41 is found between EC_{OBS} and $\overline{EC}_{AGCM}$, which is statistically significant although this skill is a bit lower than the regression model using SST anomalies associated with the NPM as shown in Fig. 10b. This discrepancy could be due to several reasons. The SAT anomalies associated with the NPM variability derived by the regression model are based on observations; therefore, other factors that are linked to the NPM that also contribute to the WACC variability are indirectly included in the regression model, such as local sea ice variability over CBS as shown in Fig. 6a. On the other hand, in addition to sea ice, part of SST variability associated with the NPM (e.g., over the CBS region where climatological sea ice is present) is also excluded in the amip_clim_polar experiment. Moreover, as previously discussed, using more model members could also improve the correlation between EC_{OBS} and $\overline{EC}_{AGCM}$ since only three AGCMs participated in the amip_clim_polar

experiment. Nevertheless, a very strong correlation ($\sim$0.75) is found between the $\overline{EC}_{AGCM}$ from the experiments amip_obs_rf and amip_clim_polar based on the three AGCM simulations (Figs. 11a,b), further suggesting that the forced WACC variability is primarily driven by the extrapolar SST variability.

It is noteworthy that the WACC variability in response to both CBS sea ice loss and the NPM-like SST pattern is systematically underestimated in models relative to its observational counterpart (Fig. 12), possibly due to lack of ocean–ice–atmosphere coupling in AGCM simulations and potential model errors (Deser et al. 2016; Mori et al. 2019a,b; Screen and Blackport 2019). It has also been argued that roles of the sea ice and SST variability in driving the WACC pattern using the coefficients of determination approach can be overestimated in observations (Screen and Blackport 2019). For example, both the observed WACC pattern and sea ice/SST anomalies over the CBS can be induced by the anomalous Alaskan high, which can be forced either by surface boundary conditions or internal variability (Guan et al. 2020a; Blackport et al. 2019). Because of the prescribed SST and sea ice patterns, these two-way interactive processes are not fully resolved in AGCMs, therefore leading to the underestimated correlations between sea ice/SST and the WACC variability (Screen and Blackport 2019; Mori et al. 2019b).

4. Summary and discussion

A "warm Arctic, cold continents" (WACC) pattern has been observed in the interannual variability and long-term trend of winter surface air temperature (SAT) anomalies over mid- to high latitudes of the Northern Hemisphere. The underlying physics regulating the WACC variability, however, remains largely elusive. In particular, most of the existing studies toward improved understanding of the WACC variability have been focusing on the Eurasian continent, and much less attention has been paid to the WACC variability over the NA sector. While limited studies indicate that both surface boundary forcing, including that due to the sea ice and SSTs, and atmospheric internal variability could be responsible for the formation of the WACC pattern over the NA sector, their relative roles are difficult to determine based on observations alone. In this study, with a specific focus on the interannual time scales, connections between the WACC variability, tropospheric atmospheric circulation, Arctic sea ice, and SST anomalies over the NP are investigated; in particular, contributions of internal drivers versus surface boundary forcing to the WACC variability over the NA sector are quantitatively estimated for the first time using a combined analysis of observations and large-ensemble AGCM simulations.

Our results confirm a crucial role of internal atmospheric variability in generating the WACC over the NA sector as previously reported (e.g., Sigmond and Fyfe 2016; Peng et al. 2018b; Sun et al. 2016). The forced WACC variance, estimated by the large-ensemble mean from AGCM simulations, explains about half of total interannual WACC variance. Optimal boundary forcing sources in generating the WACC variability over the NA sector are further identified, which are characterized by sea ice variability over CBS and a NPM-like anomalous SST pattern

over the NP basin. In contrast to a dominant role of Arctic sea ice for the WACC variability over Eurasia as previously reported, the NPM-like SST pattern is found to be the major boundary forcing in driving the WACC variability over the NA sector. While internal atmosphere variability is largely unpredictable, the identified surface boundary forcing such as the NP SST anomalies responsible for the forced WACC variability over the NA sector can serve as important predictors for seasonal climate predictions over the NA region.

As the NPM-like SST pattern involve both anomalous SST signals over the extratropical NP basin and over the TWP near 160°E (Fig. 6a), the relative importance of tropical versus extratropical SST anomalies in exciting the WACC variability over the NA sector remains uncertain (e.g., Hartmann 2015; Lee et al. 2015; Baxter and Nigam 2015). For example, Lee et al. (2015) concluded that the NPO/WP pattern across the NA sector can be forced by multiple boundary forcing including anomalous SST in the TWP and TEP, as well as over the extratropical NP. Previous observational and modeling studies also demonstrated that the extratropical SST anomalies are primarily driven by atmospheric circulation (Kumar and Chen 2018; Kumar and Wang 2015; Bretherton and Battisti 2000), which itself could be excited in responding to SST anomalies over TWP (e.g., Hartmann 2015; Sung et al. 2019), or due to the mid- to high-latitude internal dynamics, for example, associated with the NPO/WP variability (e.g., Baxter and Nigam 2015). Therefore, the relative role of tropical versus extratropical SST anomalies associated with the NPM in driving the WACC pattern over the NA sector warrants further investigations in a future study.

Significant discrepancies are found in the forced WACC signals between observations and AGCMs, with the WACC variability in response to both CBS sea ice loss and the NPM-like SST pattern systematically underestimated in model simulations. These discrepancies between models and observations could be explained by the lack of ocean–ice–atmosphere coupling in AGCMs along with model deficiencies in depicting atmospheric responses to sea ice and SST variability. In this study, a combined analysis approach using both observations and multimodel large-ensemble simulations is used to extract a leading interannual WACC pattern in model simulations similar to the observed counterpart. Many of these AGCMs have difficulty in realistically capturing the WACC pattern as the leading mode of winter SAT anomalies in response to the specified boundary forcing, possibly due to an important role of internal atmospheric processes in shaping the WACC variability as suggested by this study.

REFERENCES

Baxter, S., and S. Nigam, 2015: Key role of the North Pacific Oscillation–west Pacific pattern in generating the extreme 2013/14 North American winter. *J. Climate*, **28**, 8109–8117, https://doi.org/10.1175/JCLI-D-14-00726.1.

Benestad, R., and Coauthors, 2017: New vigour involving statisticians to overcome ensemble fatigue. *Nat. Climate Change*, **7**, 697–703, https://doi.org/10.1038/nclimate3393.

Blackport, R., J. A. Screen, K. van der Wiel, and R. Bintanja, 2019: Minimal influence of reduced Arctic sea ice on coincident cold winters in mid-latitudes. *Nat. Climate Change*, **9**, 697–704, https://doi.org/10.1038/s41558-019-0551-4.

Bretherton, C. S., and D. S. Battisti, 2000: An interpretation of the results from atmospheric general circulation models forced by the time history of the observed sea surface temperature distribution. *Geophys. Res. Lett.*, **27**, 767–770, https://doi.org/10.1029/1999GL010910.

——, C. Smith, and J. M. Wallace, 1992: An intercomparison of methods for finding coupled patterns in climate data. *J. Climate*, **5**, 541–560, https://doi.org/10.1175/1520-0442(1992)005<0541:AIOMFF>2.0.CO;2.

——, M. Widmann, V. P. Dymnikov, J. M. Wallace, and I. Bladé, 1999: The effective number of spatial degrees of freedom of a time-varying field. *J. Climate*, **12**, 1990–2009, https://doi.org/10.1175/1520-0442(1999)012<1990:TENOSD>2.0.CO;2.

Carrera, M. L., R. W. Higgins, and V. E. Kousky, 2004: Downstream weather impacts associated with atmospheric blocking over the northeast Pacific. *J. Climate*, **17**, 4823–4839, https://doi.org/10.1175/JCLI-3237.1.

Casola, J. H., and J. M. Wallace, 2007: Identifying weather regimes in the wintertime 500-hPa geopotential height field for the Pacific–North American sector using a limited-contour clustering technique. *J. Appl. Meteor. Climatol.*, **46**, 1619–1630, https://doi.org/10.1175/JAM2564.1.

Chen, H. W., F. Zhang, and R. B. Alley, 2016: The robustness of mid-latitude weather pattern changes due to Arctic sea ice loss. *J. Climate*, **29**, 7831–7849, https://doi.org/10.1175/JCLI-D-16-0167.1.

Clark, J. P., and S. Lee, 2019: The role of the tropically excited Arctic warming mechanism on the warm Arctic cold continent surface air temperature trend pattern. *Geophys. Res. Lett.*, **46**, 8490–8499, https://doi.org/10.1029/2019GL082714.

Cohen, J., and Coauthors, 2014: Recent Arctic amplification and extreme mid-latitude weather. *Nat. Geosci.*, **7**, 627–637, https://doi.org/10.1038/ngeo2234.

——, and Coauthors, 2020: Divergent consensuses on Arctic amplification influence on midlatitude severe winter weather. *Nat. Climate Change*, **10**, 20–29, https://doi.org/10.1038/s41558-019-0662-y.

Dai, Y., and B. Tan, 2019: Two types of the western Pacific pattern, their climate impacts, and the ENSO modulations. *J. Climate*, **32**, 823–841, https://doi.org/10.1175/JCLI-D-17-0618.1.

Dee, D. P., and Coauthors, 2011: The ERA-Interim reanalysis: Configuration and performance of the data assimilation system. *Quart. J. Roy. Meteor. Soc.*, **137**, 553–597, https://doi.org/10.1002/qj.828.

Deser, C., and M. L. Blackmon, 1995: On the relationship between tropical and North Pacific sea surface temperature variations. *J. Climate*, **8**, 1677–1680, https://doi.org/10.1175/1520-0442(1995)008<1677:OTRBTA>2.0.CO;2.

——, L. Sun, R. A. Tomas, and J. Screen, 2016: Does ocean coupling matter for the northern extratropical response to projected Arctic sea ice loss? *Geophys. Res. Lett.*, **43**, 2149–2157, https://doi.org/10.1002/2016GL067792.

Feldstein, S. B., 2000: The timescale, power spectra, and climate noise properties of teleconnection patterns. *J. Climate*, **13**, 4430–4440, https://doi.org/10.1175/1520-0442(2000)013<4430:TTPSAC>2.0.CO;2.

Gates, W. L., and Coauthors, 1999: An overview of the results of the Atmospheric Model Intercomparison Project (AMIP I). *Bull. Amer. Meteor. Soc.*, **80**, 29–56, https://doi.org/10.1175/1520-0477(1999)080<0029:AOOTRO>2.0.CO;2.

Gong, T., and D. Luo, 2017: Ural blocking as an amplifier of the Arctic sea ice decline in winter. *J. Climate*, **30**, 2639–2654, https://doi.org/10.1175/JCLI-D-16-0548.1.

Guan, W., X. Jiang, X. Ren, G. Chen, and Q. Ding, 2020a: Role of atmospheric variability in driving the ''warm-Arctic, cold-continent'' pattern over the North America sector and sea ice variability over the Chukchi-Bering Sea. *Geophys. Res. Lett.*, **47**, e2020GL088599, https://doi.org/10.1029/2020GL088599.

——, ——, ——, ——, P. Lin, and H. Lin, 2020b: The leading Intraseasonal variability mode of wintertime surface air temperature over the North American sector. *J. Climate*, **33**, 9287–9306, https://doi.org/10.1175/JCLI-D-20-0096.1.

Hartmann, D. L., 2015: Pacific sea surface temperature and the winter of 2014. *Geophys. Res. Lett.*, **42**, 1894–1902, https://doi.org/10.1002/2015GL063083.

Inoue, J., M. E. Hori, and K. Takaya, 2012: The role of Barents sea ice in the wintertime cyclone track and emergence of a warm-Arctic cold-Siberian anomaly. *J. Climate*, **25**, 2561–2568, https://doi.org/10.1175/JCLI-D-11-00449.1.

Kim, B.-M., S.-W. Son, S.-K. Min, J.-H. Jeong, S.-J. Kim, X. Zhang, T. Shim, and J.-H. Yoon, 2014: Weakening of the stratospheric polar vortex by Arctic sea-ice loss. *Nat. Commun.*, **5**, 4646, https://doi.org/10.1038/ncomms5646.

Kug, J.-S., J.-H. Jeong, Y.-S. Jang, B.-M. Kim, C. K. Folland, S.-K. Min, and S.-W. Son, 2015: Two distinct influences of Arctic warming on cold winters over North America and East Asia. *Nat. Geosci.*, **8**, 759–762, https://doi.org/10.1038/ngeo2517.

Kumar, A., and H. Wang, 2015: On the potential of extratropical SST anomalies for improving climate predictions. *Climate Dyn.*, **44**, 2557–2569, https://doi.org/10.1007/s00382-014-2398-8.

——, and M. Chen, 2018: Causes of skill in seasonal predictions of the Arctic Oscillation. *Climate Dyn.*, **51**, 2397–2411, https://doi.org/10.1007/s00382-017-4019-9.

Lee, M.-Y., C.-C. Hong, and H.-H. Hsu, 2015: Compounding effects of warm sea surface temperature and reduced sea ice on the extreme circulation over the extratropical North Pacific and North America during the 2013–2014 boreal winter. *Geophys. Res. Lett.*, **42**, 1612–1618, https://doi.org/10.1002/2014GL062956.

Lee, S., 2012: Testing of the tropically excited Arctic warming mechanism (TEAM) with traditional El Niño and La Niña. *J. Climate*, **25**, 4015–4022, https://doi.org/10.1175/JCLI-D-12-00055.1.

Lin, H., 2018: Predicting the dominant patterns of subseasonal variability of wintertime surface air temperature in extratropical Northern Hemisphere. *Geophys. Res. Lett.*, **45**, 4381–4389, https://doi.org/10.1029/2018GL077509.

Linkin, M. E., and S. Nigam, 2008: The North Pacific Oscillation–west Pacific teleconnection pattern: Mature-phase structure and winter impacts. *J. Climate*, **21**, 1979–1997, https://doi.org/10.1175/2007JCLI2048.1.

Matsumura, S., and Y. Kosaka, 2019: Arctic–Eurasian climate linkage induced by tropical ocean variability. *Nat. Commun.*, **10**, 3441, https://doi.org/10.1038/s41467-019-11359-7.

McCusker, K. E., J. C. Fyfe, and M. Sigmond, 2016: Twenty-five winters of unexpected Eurasian cooling unlikely due to Arctic sea-ice loss. *Nat. Geosci.*, **9**, 838–842, https://doi.org/10.1038/ngeo2820.

Mori, M., M. Watanabe, H. Shiogama, J. Inoue, and M. Kimoto, 2014: Robust Arctic sea-ice influence on the frequent Eurasian cold winters in past decades. *Nat. Geosci.*, **7**, 869–873, https://doi.org/10.1038/ngeo2277.

——, Y. Kosaka, M. Watanabe, H. Nakamura, and M. Kimoto, 2019a: A reconciled estimate of the influence of Arctic sea-ice loss on recent Eurasian cooling. *Nat. Climate Change*, **9**, 123–129, https://doi.org/10.1038/s41558-018-0379-3.

——, ——, ——, B. Taguchi, H. Nakamura, and M. Kimoto, 2019b: Reply to: Is sea-ice-driven Eurasian cooling too weak in models? *Nat. Climate Change*, **9**, 937–939, https://doi.org/10.1038/s41558-019-0636-0.

——, ——, ——, ——, ——, and ——, 2021: Reply to: Eurasian cooling in response to Arctic sea-ice loss is not proved by maximum covariance analysis. *Nat. Climate Change*, **11**, 109–111, https://doi.org/10.1038/s41558-020-00983-7.

Murray, D., and Coauthors, 2020: Facility for weather and climate assessments (FACTS): A community resource for assessing weather and climate variability. *Bull. Amer. Meteor. Soc.*, **101**, E1214–E1224, https://doi.org/10.1175/BAMS-D-19-0224.1.

Nakamura, T., K. Yamazaki, K. Iwamoto, M. Honda, Y. Miyoshi, Y. Ogawa, Y. Tomikawa, and J. Ukita, 2016: The stratospheric pathway for Arctic impacts on midlatitude climate. *Geophys. Res. Lett.*, **43**, 3494–3501, https://doi.org/10.1002/2016GL068330.

Ogawa, F., and Coauthors, 2018: Evaluating impacts of recent Arctic sea ice loss on the Northern Hemisphere winter climate change. *Geophys. Res. Lett.*, **45**, 3255–3263, https://doi.org/10.1002/2017GL076502.

Orsolini, Y. J., R. Senan, R. E. Benestad, and A. Melsom, 2012: Autumn atmospheric response to the 2007 low Arctic sea ice extent in coupled ocean–atmosphere hindcasts. *Climate Dyn.*, **38**, 2437–2448, https://doi.org/10.1007/s00382-011-1169-z.

Overland, J. E., K. R. Wood, and M. Wang, 2011: Warm Arctic–cold continents: Climate impacts of the newly open Arctic Sea. *Polar Res.*, **30**, 15787, https://doi.org/10.3402/polar.v30i0.15787.

Palmer, T., 2014: Record-breaking winters and global climate change. *Science*, **344**, 803–804, https://doi.org/10.1126/science.1255147.

Park, H.-S., S. Lee, S.-W. Son, S. B. Feldstein, and Y. Kosaka, 2015: The impact of poleward moisture and sensible heat flux on Arctic winter sea ice variability. *J. Climate*, **28**, 5030–5040, https://doi.org/10.1175/JCLI-D-15-0074.1.

Park, J.-Y., S.-W. Yeh, and J.-S. Kug, 2012: Revisited relationship between tropical and North Pacific sea surface temperature variations. *Geophys. Res. Lett.*, **39**, L02703, https://doi.org/10.1029/2011GL050005.

Peings, Y., and G. Magnusdottir, 2014: Forcing of the wintertime atmospheric circulation by the multidecadal fluctuations of the North Atlantic Ocean. *Environ. Res. Lett.*, **9**, 034018, https://doi.org/10.1088/1748-9326/9/3/034018.

Peng, P., A. Kumar, and Z.-Z. Hu, 2018a: What drove the Pacific and North America climate anomalies in winter 2014/15?

Climate Dyn., **51**, 2667–2679, https://doi.org/10.1007/s00382-017-4035-9.

——, ——, M. Chen, Z.-Z. Hu, and B. Jha, 2018b: Was the North American extreme climate in winter 2013/14 a SST forced response? *Climate Dyn.*, **52**, 3099–3110, https://doi.org/10.1007/s00382-018-4314-0.

Rayner, N. A., D. E. Parker, E. B. Horton, C. K. Folland, L. V. Alexander, D. P. Rowell, E. C. Kent, and A. Kaplan, 2003: Global analyses of sea surface temperature, sea ice, and night marine air temperature since the late nineteenth century. *J. Geophys. Res.*, **108**, 4407, https://doi.org/10.1029/2002JD002670.

Screen, J. A., and R. Blackport, 2019: Is sea-ice-driven Eurasian cooling too weak in models? *Nat. Climate Change*, **9**, 934–936, https://doi.org/10.1038/s41558-019-0635-1.

Seager, R., M. Hoerling, S. Schubert, H. Wang, B. Lyon, A. Kumar, J. Nakamura, and N. Henderson, 2015: Causes of the 2011–14 California drought. *J. Climate*, **28**, 6997–7024, https://doi.org/10.1175/JCLI-D-14-00860.1.

Semenov, V. A., and M. Latif, 2015: Nonlinear winter atmospheric circulation response to Arctic sea ice concentration anomalies for different periods during 1966–2012. *Environ. Res. Lett.*, **10**, 054020, https://doi.org/10.1088/1748-9326/10/5/054020.

Sigmond, M., and J. C. Fyfe, 2016: Tropical Pacific impacts on cooling North American winters. *Nat. Climate Change*, **6**, 970–974, https://doi.org/10.1038/nclimate3069.

Sorokina, S. A., C. Li, J. J. Wettstein, and N. G. Kvamstø, 2016: Observed atmospheric coupling between Barents sea ice and the warm-Arctic cold-Siberian anomaly pattern. *J. Climate*, **29**, 495–511, https://doi.org/10.1175/JCLI-D-15-0046.1.

Straus, D. M., S. Corti, and F. Molteni, 2007: Circulation regimes: Chaotic variability versus SST-forced predictability. *J. Climate*, **20**, 2251–2272, https://doi.org/10.1175/JCLI4070.1.

Sun, L., J. Perlwitz, and M. Hoerling, 2016: What caused the recent "warm Arctic, cold continents" trend pattern in winter temperatures? *Geophys. Res. Lett.*, **43**, 5345–5352, https://doi.org/10.1002/2016GL069024.

——, D. Allured, M. Hoerling, L. Smith, J. Perlwitz, D. Murray, and J. Eischeid, 2018: Drivers of 2016 record Arctic warmth assessed using climate simulations subjected to factual and counterfactual forcing. *Wea. Climate Extremes*, **19**, 1–9, https://doi.org/10.1016/j.wace.2017.11.001.

Sung, M.-K., H.-Y. Jang, B.-M. Kim, S.-W. Yeh, Y.-S. Choi, and C. Yoo, 2019: Tropical influence on the North Pacific Oscillation

drives winter extremes in North America. *Nat. Climate Change*, **9**, 413–418, https://doi.org/10.1038/s41558-019-0461-5.

Takaya, K., and H. Nakamura, 2001: A formulation of a phase-independent wave-activity flux for stationary and migratory quasigeostrophic eddies on a zonally varying basic flow. *J. Atmos. Sci.*, **58**, 608–627, https://doi.org/10.1175/1520-0469(2001)058<0608:AFOAPI>2.0.CO;2.

Tanaka, S., K. Nishii, and H. Nakamura, 2016: Vertical structure and energetics of the western Pacific teleconnection pattern. *J. Climate*, **29**, 6597–6616, https://doi.org/10.1175/JCLI-D-15-0549.1.

Tang, Q., X. Zhang, X. Yang, and J. A. Francis, 2013: Cold winter extremes in northern continents linked to Arctic sea ice loss. *Environ. Res. Lett.*, **8**, 014036, https://doi.org/10.1088/1748-9326/8/1/014036.

Teng, H., and G. Branstator, 2017: Causes of extreme ridges that induce California droughts. *J. Climate*, **30**, 1477–1492, https://doi.org/10.1175/JCLI-D-16-0524.1.

Vimont, D. J., J. M. Wallace, and D. S. Battisti, 2003: The seasonal footprinting mechanism in the Pacific: Implications for ENSO. *J. Climate*, **16**, 2668–2675, https://doi.org/10.1175/1520-0442(2003)016<2668:TSFMIT>2.0.CO;2.

Wang, S. Y., L. Hipps, R. R. Gillies, and J.-H. Yoon, 2014: Probable causes of the abnormal ridge accompanying the 2013–2014 California drought: ENSO precursor and anthropogenic warming footprint. *Geophys. Res. Lett.*, **41**, 3220–3226, https://doi.org/10.1002/2014GL059748.

Watson, P. A. G., A. Weisheimer, J. R. Knight, and T. N. Palmer, 2016: The role of the tropical west Pacific in the extreme Northern Hemisphere winter of 2013/2014. *J. Geophys. Res.*, **121**, 1698–1714, https://doi.org/10.1002/2015JD024048.

Xue, D., J. Lu, L. Sun, G. Chen, and Y. Zhang, 2017: Local increase of anticyclonic wave activity over northern Eurasia under amplified Arctic warming. *Geophys. Res. Lett.*, **44**, 3299–3308, https://doi.org/10.1002/2017GL072649.

Zappa, G., P. Ceppi, and T. G. Shepherd, 2021: Eurasian cooling in response to Arctic sea-ice loss is not proved by maximum covariance analysis. *Nat. Climate Change*, **11**, 106–108, https://doi.org/10.1038/s41558-020-00982-8.

Zhang, P., Y. Wu, I. R. Simpson, K. L. Smith, X. Zhang, B. De, and P. Callaghan, 2018: A stratospheric pathway linking a colder Siberia to Barents-Kara Sea sea ice loss. *Sci. Adv.*, **4**, eaat6025, https://doi.org/10.1126/sciadv.aat6025.